Wideband Modeling of Graphene Using the Finite-Difference Time-Domain Method

Vahid Nayyeri, *Student Member, IEEE*, Mohammad Soleimani, and Omar M. Ramahi, *Fellow, IEEE*

***Abstract*—In this paper, we present a method to incorporate the intraband and interband terms of the surface conductivity of graphene into the finite-difference time-domain (FDTD) method. The method is based on approximating the surface resistivity of graphene by a series of partial fractions in terms of real or complex conjugate pole–residue pairs. Then, a discrete time-domain surface boundary condition at the graphene sheet is generated, which is then incorporated within the FDTD method using the infinitesimally thin sheet formulation. Numerical examples are presented to validate and demonstrate the capabilities and advantages of the proposed approach.**

***Index Terms*—Finite-difference time-domain (FDTD), graphene, surface boundary condition, surface conductivity.**

I. Introduction

GRAPHENE, a planar monoatomic layer of carbon bonded in a hexagonal structure, has been shown to provide unusual mechanical, electric, magnetic, and thermal properties [1]. Numerous applications of graphene in a wide spectral range (from terahertz to X-rays) have recognized it as a versatile optical material [2], [3]. In many of these applications, electromagnetic properties of graphene are of interest. In most practical problems, analytic solution of Maxwell's equations is impossible; thus, numerical simulation methods have to be used. Hence, geraphene has been modeled in various kind of numerical methods such as the method of moment (MoM) [4], the finite-element method (FEM) [5], and the FDTD method [6]–[11]. Among the available numerical methods used to solve Maxwell equations, time-domain methods have specific advantages that relate primarily to computing resources and simulation time, particularly when a wide range of frequency is of interest. (It must be emphasized, however, that the advantages of time-domain methods are typically associated with specific problems, such as transients, and cannot be assumed to be universal advantages within all numerical methods.) Specifically, the finite-difference time-domain (FDTD) method is highly robust with advantages such as simplicity, generality, and ease of implementation for simulation of optical components [12]. Accordingly for modeling of graphene in a wide frequency band, the FDTD method could be a wise choice.

Graphene has been modeled in the FDTD method using the following three implementations:

1) using a standard FDTD method with high discretization density for the fields inside the graphene sheet [6]–[9];
2) using the subcell FDTD method [10];
3) by splitting the magnetic fields tangential to the graphene sheet and using the surface boundary condition (SBC) [11].

The first two approaches treated graphene as a thin volumetric layer (occupying some, as in the first approach, or a fraction, as in the second one, of the FDTD cells). Considering that graphene is a one-atom thick layer, the standard FDTD approach calls for extremely fine spatial discretization inside the graphene layer. Consequently, the methods require extremely fine time discretization to guarantee stability, thus incurring large computational resources. On the other hand, the second approach, which uses the subcell FDTD method, requires a special type of PML to model infinitely thin sheets [13]. In the third approach, graphene was modeled as a conductive *surface*, instead of conductive volume. By implementing a surface boundary condition (SBC) in the FDTD method and using the surface conductivity of graphene, updating equations at and in the proximity of the graphene surface can be derived. The third approach did not suffer from constraint on the FDTD cell size or the constraints of subcell methods, and hence is highly effective.

The surface conductivity of graphene had been commonly expressed by Kubo formula consisting of two contributions representing the electronic intraband relaxation and interband transitions [14]. Below a transition band, typically in the mid-infrared region, the intraband contribution is the dominant term of the conductivity, with a real part that is negligible and an imaginary part that attains negative values. Hence, graphene can provide the features of a low-loss material with a negative real part of the permittivity. In the transition band and beyond, the interband contribution, which has a positive imaginary part and a considerable real part, has to be taken into account. In many applications, the behavior of graphene in the transition band is of interest, especially in supporting transverse-magnetic (TM) electromagnetic surface-plasmon polariton (SPP) surface waves [15].

The intraband contribution is expressed by a simple Drude-like expression, while the interband one has a complex expression [16]. Therefore, the intraband term can be directly implemented in the FDTD method, whereas the interband term cannot. Hence, in the earlier works, only the intraband term of graphene conductivity was considered [6], [7], [10], [11]. Recently, the

Manuscript received May 20, 2013; revised September 13, 2013; accepted September 13, 2013. Date of publication September 18, 2013; date of current version November 25, 2013.

V. Nayyeri is with the Department of Electrical and Computer Engineering, University of Waterloo, Waterloo, ON N2L 3G1, Canada, and also with the School of Electrical Engineering, Iran University of Science and Technology, Tehran 16844, Iran (e-mail: nayyeri@ieee.org).

M. Soleimani is with the School of Electrical Engineering, Iran University of Science and Technology, Tehran 16844, Iran (e-mail: soleimani@iust.ac.ir).

O. M. Ramahi is with the Department of Electrical and Computer Engineering, University of Waterloo, ON N2L 3G1, Canada (e-mail: oramahi@uwaterloo.ca).

Color versions of one or more of the figures in this paper are available online at http://ieeexplore.ieee.org.

Digital Object Identifier 10.1109/TAP.2013.2282535

conductivity of graphene with both intraband and interband contributions was modeled in the standard FDTD method [8], [9]. In these works, however, the surface conductivity of graphene was first converted to volumetric conductivity (permittivity), then, partial fractional models were used to approximate the conductivity. The implementation of the volumetric conductivity given by a partial fractional model in the standard FDTD follows in a straightforward fashion. However, as mentioned above, using the standard FDTD method incurs heavy computational burden and long simulation time.

This paper presents a method to incorporate both the intraband and interband terms of graphene conductivity in a highly efficient SBC-based FDTD method. Earlier methods proposed for modeling complex dispersive media, such as [17], cannot be applied for this purpose, since in those methods, the volumetric conductivity of a medium is applied in the FDTD method. In the SBC-based FDTD approach, however, the *surface* resistivity of graphene would be required. Therefore, our approach in this work is to incorporate a well-known rational model consisting of real and complex-conjugate pole-residue pairs, which was used for approximation of volumetric permittivity of dispersive media, to approximating the surface resistivity of graphene. Then, a method is proposed to implement the rational model into the SBC-based FDTD method. A full validation of the method is presented.

II. Method Development

Graphene is analytically modeled as an infinitesimally thin, local two-sided surface characterized by a surface conductivity σ_g, which can be expressed using the well-known Kubo formalism. In the absence of magnetostatic bias and spatial dispersion, the surface conductivity of chemically doped and/or electrostatically biased graphene is a scalar function of frequency ω, chemical potential μ_c (which can be controlled by either an applied electrostatic bias or chemical doping), phenomenological scattering rate Γ (or relaxation time $\tau = 1/2\Gamma$), and temperature T as

$$\sigma_g(\omega,\mu_c,\Gamma,T) = \frac{je^2(\omega - j2\Gamma)}{\pi\hbar^2} \left[\frac{1}{(\omega - j2\Gamma)^2}\int_0^\infty \varepsilon\left(\frac{\partial f_d(\varepsilon)}{\partial\varepsilon} - \frac{\partial f_d(-\varepsilon)}{\partial\varepsilon}\right)d\varepsilon - \int_0^\infty \frac{f_d(-\varepsilon) - f_d(\varepsilon)}{(\omega - j2\Gamma)^2 - 4\left(\frac{\varepsilon}{\hbar}\right)^2}d\varepsilon\right] \quad (1)$$

where ε is the energy, $\hbar$ is the reduced Planck constant, $-e$ is the charge of an electron, k_B is the Boltzmann's constant, and $f_d = \left(e^{(\varepsilon-|\mu_c|)/k_BT}+1\right)^{-1}$ is the Fermi–Dirac Dirac distribution [14], [18]. In (1), the conductivity of graphene consists of two terms. The first term is due to the intraband contributions. This term can be evaluated as

$$\sigma_{\text{intra}} = \frac{e^2k_BT}{\pi\hbar^2(2\Gamma + j\omega)}\left[\frac{\mu_c}{k_BT} + 2\ln\left(\exp\left\{-\frac{\mu_c}{k_BT}\right\}+1\right)\right]. \quad (2)$$

The second term is due to the interband contributions. In general, the interband term must be evaluated numerically, however, for $k_BT \ll |\mu_c|, \hbar\omega$ can be approximated by its value at $T = 0$ as a logarithmic function [16]. It is shown that, for the frequency $\omega \ll 2\mu_c/\hbar$, the interband term is negligible and the intraband term is dominant; however, from $\omega \approx 2\mu_c/\hbar$, the interband term cannot be neglected [16].

The fields at the graphene sheet obey the surface boundary condition

$$\mathbf{E}_t(\omega) = \rho_g(\omega)\,\hat{n} \times \left[{}^2\mathbf{H}(\omega) - {}^1\mathbf{H}(\omega)\right] \quad (3)$$

where $\mathbf{E}_t$ is the tangential component of the electric field at the sheet, $\rho_g = 1/\sigma_g$ is the surface resistivity of graphene, $\hat{n}$ denotes the unit vector normal to the sheet (from side 1 to side 2), and ${}^1\mathbf{H}$ and ${}^2\mathbf{H}$ are magnetic fields at the two sides of the sheet. To implement the graphene model into the FDTD method, (3) needs to be converted into a discrete-time relation. This would require substituting (1) into (3). The intraband conductivity, as expressed by a Drude-like expression in (2), lends itself to a direct conversion of the frequency domain equation in (3) [11]; however, due to the complexity of the interband term, (3) cannot be *directly* converted into a discrete-time domain relation. Therefore, a sum of partial fractions in terms of real and/or complex-conjugate pole–residue pairs, which had been used to approximate complex functions of frequency [19] (and has been applied for characterizing volumetric permittivity of complex dispersive media in optical range [17]), can be used to approximate the surface resistivity of graphene as

$$\rho_g(\omega) \approx \rho_\infty + \sum_{k=1}^{N}\rho_k(\omega) \quad (4)$$

where ρ_∞ is the surface resistivity at infinite frequency

$$\rho_k(\omega) = \begin{cases} \frac{r_k}{j\omega - p_k}; & p_k \text{ and } r_k \text{ are real} \\ \frac{r_k}{j\omega - p_k} + \frac{r_k{}^*}{j\omega - p_k{}^*}; & p_k \text{ and } r_k \text{ are complex} \end{cases} \quad (5)$$

and p_k and r_k are the poles and residues, respectively. The approximation parameters in (4) and(5) can be extracted using vector fitting [19] or curve fitting [20]. (To insure causality and stability, positive values for the real part of p_k should be avoided [17].) Now, the approximate form in (4) makes possible the conversion from frequency domain to time domain. By substituting (4) in (3), we have

$$\mathbf{E}_t(\omega) = \mathbf{E}_\infty(\omega) + \sum_{k=1}^{N}\mathbf{E}_k(\omega) \quad (6)$$

where

$$\mathbf{E}_\infty(\omega) = \rho_\infty\hat{n} \times \left[{}^2\mathbf{H}(\omega) - {}^1\mathbf{H}(\omega)\right] \quad (7)$$

and

$$\mathbf{E}_k(\omega) = \rho_k(\omega)\,\hat{n} \times \left[{}^2\mathbf{H}(\omega) - {}^1\mathbf{H}(\omega)\right]. \quad (8)$$

Equation (7) can be easily converted into time domain as

$$\mathbf{E}_\infty(t) = \rho_\infty\hat{n} \times \left[{}^2\mathbf{H}(t) - {}^1\mathbf{H}(t)\right].$$

Converting the above relation into discrete time-domain equation and enforcing the equation at the discrete time step n,

$$\mathbf{E}_\infty{}^n = \rho_\infty \hat{n} \times \left[{}^2\mathbf{H}^n - {}^1\mathbf{H}^n\right].$$

For implementation into a standard Yee-type FDTD method where the $\mathbf{E}$ and $\mathbf{H}$ fields are evaluated at one-half time step apart, we use the following time-averages for the magnetic fields at time steps $n-1/2$ and $n+1/2$:

$$\begin{aligned} {}^1\mathbf{H}^n &= \frac{1}{2}\left({}^1\mathbf{H}^{n-1/2} + {}^1\mathbf{H}^{n+1/2}\right) \\ {}^2\mathbf{H}^n &= \frac{1}{2}\left({}^2\mathbf{H}^{n-1/2} + {}^2\mathbf{H}^{n+1/2}\right). \end{aligned}$$

Finally, we have

$$\mathbf{E}_\infty{}^n = \frac{1}{2}\rho_\infty \hat{n} \times \left\{\left[{}^2\mathbf{H} - {}^1\mathbf{H}\right]^{n-1/2} + \left[{}^2\mathbf{H} - {}^1\mathbf{H}\right]^{n+1/2}\right\}. \tag{9}$$

Now, we turn our attention to $\mathbf{E}_k(\omega)$. Considering the definition of $\rho_k(\omega)$ in (5), (8) can also be converted into a discrete-time domain relation. Caution must be exercised here as there are two distinct possibilities for the types of zeros and poles that characterize $\rho_k(\omega)$. Let us first assume real values for r_k and p_k in $\rho_k(\omega)$. By substituting (5) in (8), we have

$$(j\omega - p_k)\,\mathbf{E}_k(\omega) = r_k \hat{n} \times \left[{}^2\mathbf{H}(\omega) - {}^1\mathbf{H}(\omega)\right].$$

Converting the expression from frequency domain into the time domain, we have

$$\frac{\partial}{\partial t}\mathbf{E}_k(t) - p_k \mathbf{E}_k(t) = r_k \hat{n} \times \left[{}^2\mathbf{H}(t) - {}^1\mathbf{H}(t)\right].$$

Next, we convert the above relation into a discrete-time equation and enforce the equation at $n-1/2$ while using the central difference scheme for the time derivative at $n-1/2$

$$\frac{\mathbf{E}_k{}^n - \mathbf{E}_k{}^{n-1}}{\Delta t} - p_k \mathbf{E}_k{}^{n-1/2} = r_k\, \hat{n} \times \left[{}^2\mathbf{H} - {}^1\mathbf{H}\right]^{n-1/2}$$

where Δt is the discrete time step. Finally, we express $\mathbf{E}_k$ at time step $n-1/2$ as the average of the fields at time steps n and $n-1$:

$$\frac{\mathbf{E}_k{}^n - \mathbf{E}_k{}^{n-1}}{\Delta t} - p_k \frac{\mathbf{E}_k{}^n + \mathbf{E}_k{}^{n-1}}{2} = r_k\, \hat{n} \times \left[{}^2\mathbf{H} - {}^1\mathbf{H}\right]^{n-1/2}.$$

Rearranging, we obtain

$$\mathbf{E}_k{}^n = e_k\, \mathbf{E}_k{}^{n-1} + h_k\, \hat{n} \times \left[{}^2\mathbf{H} - {}^1\mathbf{H}\right]^{n-1/2}$$

where

$$e_k = \frac{1 + \frac{p_k \Delta t}{2}}{1 - \frac{p_k \Delta t}{2}}, \quad h_k = \frac{r_k \Delta t}{1 - \frac{p_k \Delta t}{2}}.$$

For the case where r_k and p_k are complex, substituting $\rho_k(\omega)$ (given by (5)) in (8), we have

$$\mathbf{E}_k(\omega) = \left(\frac{r_k}{j\omega - p_k} + \frac{r_k{}^*}{j\omega - p_k{}^*}\right) \hat{n} \times \left[{}^2\mathbf{H}(\omega) - {}^1\mathbf{H}(\omega)\right].$$

In the above equation, $\mathbf{E}_k(\omega)$ can be expressed as the sum of two terms:

$$\mathbf{E}_k(\omega) = \mathbf{E}_k^1(\omega) + \mathbf{E}_k^2(\omega) \tag{10}$$

where

$$\begin{aligned} \mathbf{E}_k^1(\omega) &= \frac{r_k}{j\omega - p_k} \hat{n} \times \left[{}^2\mathbf{H}(\omega) - {}^1\mathbf{H}(\omega)\right] \\ \mathbf{E}_k^2(\omega) &= \frac{r_k{}^*}{j\omega - p_k{}^*} \hat{n} \times \left[{}^2\mathbf{H}(\omega) - {}^1\mathbf{H}(\omega)\right]. \end{aligned} \tag{11}$$

Converting (10) and (11) into discrete time-domain equations (in a similar way to the case where r_k and p_k were real values), we can express $\mathbf{E}_k{}^n$ as the sum of two *non-observable* field terms

$$\mathbf{E}_k{}^n = \mathbf{E}_k^1{}^n + \mathbf{E}_k^2{}^n$$

where

$$\begin{aligned} \mathbf{E}_k^1{}^n &= e_k\, \mathbf{E}_k^1{}^{n-1} + h_k\, \hat{n} \times \left[{}^2\mathbf{H} - {}^1\mathbf{H}\right]^{n-1/2} \\ \mathbf{E}_k^2{}^n &= e_k^*\, \mathbf{E}_k^2{}^{n-1} + h_k^*\, \hat{n} \times \left[{}^2\mathbf{H} - {}^1\mathbf{H}\right]^{n-1/2}. \end{aligned} \tag{12}$$

Since the coefficients of (12) are complex conjugate pairs and the equations have same real initial values, we have

$$\mathbf{E}_k^1{}^n = \{\mathbf{E}_k^2{}^n\}^*$$

hence

$$\mathbf{E}_k{}^n = 2\Re\left\{\mathbf{E}_k^1{}^n\right\}.$$

Consequently, we can present the discrete-time domain general field update equation as

$$\mathbf{E}_k{}^n = \delta_k\, \Re\left\{e_k\, \mathbf{E}_k{}^{n-1} + h_k\, \hat{n} \times \left[{}^2\mathbf{H} - {}^1\mathbf{H}\right]^{n-1/2}\right\} \tag{13}$$

where

$$\delta_k = \begin{cases} 1; & r_k \text{ and } p_k \text{ real} \\ 2; & r_k \text{ and } p_k \text{ complex.} \end{cases}$$

Finally, representing (6) in discrete-time domain

$$\mathbf{E}_t{}^n = \mathbf{E}_\infty{}^n + \sum_{k=1}^{N} \mathbf{E}_k{}^n. \tag{14}$$

Substituting (9) in (14), we have

$$\begin{aligned} \mathbf{E}_t{}^n = \frac{\rho_\infty}{2} \hat{n} \times &\left\{\left[{}^2\mathbf{H} - {}^1\mathbf{H}\right]^{n+1/2} + \left[{}^2\mathbf{H} - {}^1\mathbf{H}\right]^{n-1/2}\right\} \\ &+ \sum_{k=1}^{N} \mathbf{E}_k{}^n \end{aligned} \tag{15}$$

where $\mathbf{E}_k{}^n$ is given in (13).

Equation (15) in essence represents a surface boundary condition (SBC), which can be implemented by using the recently proposed method for incorporating an SBC into an FDTD method [11]. The implementation is carried out by defining magnetic and electric fields at both sides of the graphene sheet as shown in the 3D FDTD cell in Fig. 1. Notice how in Fig. 1,

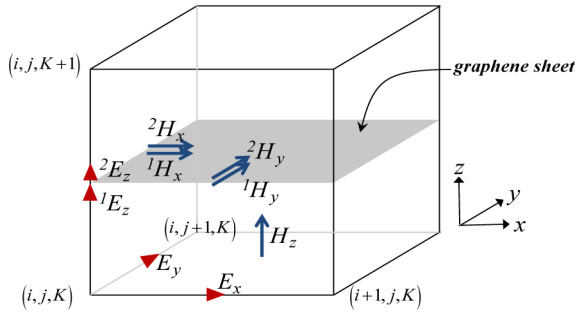

Fig. 1. Expressing normal electric and tangential magnetic fields on both sides of the graphene sheet in a 3-D FDTD cell.

H_x, H_y, and E_z are defined immediately to the bottom and top sides of the sheet. Next, Faraday's law $\partial\mathbf{B}/\partial t = -\nabla\times\mathbf{E}$ is discretized and enforced at time step n and spatial grid $(i, j+1/2, K+1/2)$ and $(i+1/2, j, K+1/2)$ for the x- and y-component, respectively. The central difference scheme is used for time derivative and spatial derivatives along x- and y-directions and backward and forward difference schemes are used for the spatial derivatives along the z-direction (normal to the surface). For the x-component of magnetic field, we obtain [11]

$$\begin{aligned}
&\frac{\mu_1}{\Delta t}\left[{}^1H_{x\,(i,j+1/2,K+1/2)}^{\;n+1/2} - {}^1H_{x\,(i,j+1/2,K+1/2)}^{\;n-1/2}\right] = \\
&\quad\frac{2}{\Delta z}\left[E_{y\,(i,j+1/2,K+1/2)}^{\;n} - E_{y\,(i,j+1/2,K)}^{\;n}\right] \\
&\quad-\frac{1}{\Delta y}\left[{}^1E_{z\,(i,j+1,K+1/2)}^{\;n} - {}^1E_{z\,(i,j,K+1/2)}^{\;n}\right], \\
&\frac{\mu_2}{\Delta t}\left[{}^2H_{x\,(i,j+1/2,K+1/2)}^{\;n+1/2} - {}^2H_{x\,(i,j+1/2,K+1/2)}^{\;n-1/2}\right] = \\
&\quad\frac{2}{\Delta z}\left[E_{y\,(i,j+1/2,K+1)}^{\;n} - E_{y\,(i,j+1/2,K+1/2)}^{\;n}\right] \\
&\quad-\frac{1}{\Delta y}\left[{}^2E_{z\,(i,j+1,K+1/2)}^{\;n} - {}^2E_{z\,(i,j,K+1/2)}^{\;n}\right] \qquad (16)
\end{aligned}$$

where μ_1 and μ_2 are the permeability of the media to the bottom and top sides of the sheet, and Δz and Δy are the mesh size in the z- and y-direction, respectively.

It is noted that mixing central with backward/forward difference schemes had been used to model boundary conditions in previous work and did not result in instability [11], [21]. Nevertheless, as will be seen in Section III below, the formulations presented here did not result in any instability. Now, in the above equations, the $E_{y\,(i,j+1/2,K+1/2)}^{\;n}$, which is the tangential field on the graphene surface, can be substituted using (15) by

$$\begin{aligned}
&E_{y\,(i,j+1/2,K+1/2)}^{\;n} = \\
&\quad\frac{\rho_\infty}{2}\left\{\left[{}^2H_x - {}^1H_x\right]^{n+1/2}\right. \\
&\qquad\left.+\left[{}^2H_x - {}^1H_x\right]^{n-1/2}\right\}_{(i,j+1/2,K+1/2)} \\
&\quad+\sum_{k=1}^{N} E_{k,y\,(i,j+1/2,K+1/2)}^{\;n}, \qquad (17)
\end{aligned}$$

where $E_{k,y}{}^n$ is the y-component of $\mathbf{E}_k{}^n$ given in (13). Substituting (17) in (16) and collecting ${}^1H_x{}^{n+1/2}$ and ${}^2H_x{}^{n+1/2}$ at the left sides of equations, we obtain the following system:

$$\begin{bmatrix} 1 & -c_1 \\ -c_2 & 1 \end{bmatrix}\begin{bmatrix} {}^1H_x \\ {}^2H_x \end{bmatrix}_{(i,j+1/2,K+1/2)}^{n+1/2} = \begin{bmatrix} {}^1F \\ {}^2F \end{bmatrix}_{(i,j+1/2,K+1/2)}^{n},$$

where

$$c_1 = \frac{\Delta t}{\mu_1\,\Delta z\,\sigma_\infty + \Delta t}, \quad c_2 = \frac{\Delta t}{\mu_2\,\Delta z\,\sigma_\infty + \Delta t}$$

and $\sigma_\infty = 1/\rho_\infty$. ${}^1F^n$ and ${}^2F^n$ are functions of the field components at time steps n and $n-1/2$ defined as

$$\begin{aligned}
&{}^1F_{(i,j+1/2,K+1/2)}^{\;n} = \\
&\quad f_{h11}\,{}^1H_{x\,(i,j+1/2,K+1/2)}^{\;n-1/2} + f_{h12}\,{}^2H_{x\,(i,j+1/2,K+1/2)}^{\;n-1/2} \\
&\quad-f_{e1}\left[2E_{y\,(i,j+1/2,K)}^{\;n} - 2\sum_{k=1}^{N} E_{k,y\,(i,j+1/2,K+1/2)}^{\;n}\right. \\
&\qquad\left.+\frac{\Delta z}{\Delta y}\left[{}^1E_{z\,(i,j+1,K+1/2)}^{\;n} - {}^1E_{z\,(i,j,K+1/2)}^{\;n}\right]\right], \\
&{}^2F_{(i,j+1/2,K+1/2)}^{\;n} = \\
&\quad f_{h21}\,{}^1H_{x\,(i,j+1/2,K+1/2)}^{\;n-1/2} + f_{h22}\,{}^2H_{x\,(i,j+1/2,K+1/2)}^{\;n-1/2} \\
&\quad-f_{e2}\left[-2E_{y\,(i,j+1/2,K+1)}^{\;n} + 2\sum_{k=1}^{N} E_{k,y\,(i,j+1/2,K+1/2)}^{\;n}\right. \\
&\qquad\left.+\frac{\Delta z}{\Delta y}\left[{}^2E_{z\,(i,j+1,K+1/2)}^{\;n} - {}^2E_{z\,(i,j,K+1/2)}^{\;n}\right]\right] \qquad (18)
\end{aligned}$$

where $f_{e1} = \sigma_\infty c_1$, $f_{e2} = \sigma_\infty c_2$, $f_{h11} = 1 - 2c_1$, $f_{h22} = 1 - 2c_2$, $f_{h12} = c_1$, and $f_{h21} = c_2$.

Solving the system gives

$$\begin{aligned}
{}^1H_x{}^{n+1/2} &= \frac{1}{1-c_1c_2}\left({}^1F^n + c_1\,{}^2F^n\right) \\
{}^2H_x{}^{n+1/2} &= \frac{1}{1-c_1c_2}\left({}^2F^n + c_2\,{}^1F^n\right). \qquad (19)
\end{aligned}$$

In summary, updating of ${}^1H_x$ and ${}^2H_x$ is performed using the following steps:

1) updating $E_{k,y}$ using (13);
2) updating ${}^1F$ and ${}^2F$ using (18);
3) updating ${}^1H_x$ and ${}^2H_x$ using (19).

A similar procedure can be applied for updating ${}^1H_y$ and ${}^2H_y$. Once the tangential magnetic fields at the graphene sheet are updated, they can be used for updating the normal components of the electric field at the bottom and top sides of the sheet (i.e., ${}^1E_z$ and ${}^2E_z$) using the classical Yee's algorithm.

We note that the presence of magnetostatic bias and spatial dispersion is not considered in this paper [18], [22]. Under these scenarios, the fields updating equations at the surface (graphene layer) need to be modified, which could be the subject of a future work due to interesting features of spatially dispersive and nonreciprocal graphene demonstrated in recent publications, such as [23]–[27].

III. Numerical Examples and Validation

Two graphene layers with $\Gamma = 0.43$ meV/$\hbar$ at temperature $T = 30$ K are considered; one with $\mu_c = 150$ meV and the

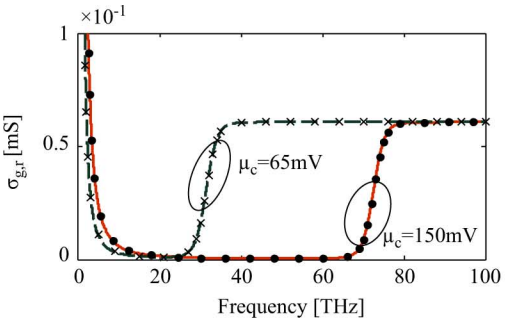

Fig. 2. (a) Real and (b) imaginary parts of the surface conductivity of graphene for two different values of chemical potential; the solid and dashed lines (red and green) show the conductivity determined by Kubo formula, and the marks (dots and crosses) show the approximated conductivity using (4) where the pole–residue pairs are given in Tables II and II. (c) Error between Kubo formula and (4).

other with $\mu_c = 65$ meV. The surface resistivity of the graphene layers ($\rho_g = 1/\sigma_g$) is first evaluated by (1) and then is approximated by (4), where the method of [20] is used to extract the approximation parameters, ρ_∞, r_k and p_k. It is found that considering seven pole–residue pairs (one real and three complex conjugate pairs) gives good approximation in the frequency range of 1–100 THz. The extracted values of the poles and residues are given in Tables I and II, where $\rho_\infty = 1.6794 \times 10^4$ and $\rho_\infty = 1.6433 \times 10^4$ for $\mu_c = 150$ meV and $\mu_c = 65$ meV, respectively. To demonstrate the accuracy of the approximation, the surface conductivities $\sigma_{\text{approx}} = 1/\rho_{\text{approx}}$ as calculated using the rational function expressions and those calculated using Kubo formula are shown in Fig. 2. Very strong agreements is observed between the two expressions over the range 1–100 THz such that the maximum error between them is less than 1.6% (see Fig. 2(c)). Notice that the phenomenological scattering rate Γ is assumed to be constant versus frequency. However, for more accurate modeling of "highly

TABLE I
EXTRACTED VALUES OF POLES (p_k) AND RESIDUES (r_k) FOR A GRAPHENE SHEET WITH $\mu_c = 150$ meV, $\Gamma = 0.43$ meV/$\hbar$, AND $T = 30$ K

k	$p_k \times 10^{-14}$	$r_k \times 10^{-18}$
1	-5.9269	-4.8350
2,3	-2.0968 $\pm$ j4.2234	-0.2887 $\pm$ j 1.5547
4,5	-0.5192 $\pm$ j4.4619	-0.1765 $\pm$ j0.4593
6,7	-0.0132 $\pm$ j3.7901	2.4461 $\pm$ j0.0067

TABLE II
EXTRACTED VALUES OF POLES (p_k) AND RESIDUES (r_k) FOR A GRAPHENE SHEET WITH $\mu_c = 65$ meV, $\Gamma = 0.43$ meV/$\hbar$, AND $T = 30$ K

k	$p_k \times 10^{-14}$	$r_k \times 10^{-18}$
1,2	-0.4549 $\pm$ j1.8648	-1.2684 $\pm$ j 2.6891
3,4	-0.0199 $\pm$ j 1.6234	9.8688 $\pm$ j0.7526
5,6	-0.9675 $\pm$ j 1.2734	-4.6157 $\pm$ j3.2365
7	-1.3870	-7.9723

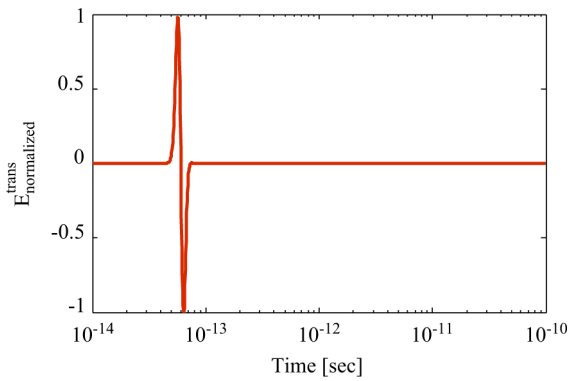

Fig. 3. Normalized transmitted electric field through the graphene layer with $\mu_c = 150$ meV.

doped" graphene in the infrared regime, a frequency-dependent phenomenological scattering rate could be considered [28]. We emphasize that the series model given in (4) and (5) can be applied to approximate different physical models used for the conductivity of graphene. Hence, the applicability of the presented FDTD method based on the series approximation is not restricted to the constant values of phenomenological scattering rate.

As a first example, by applying the extracted parameters in the proposed method, we validate the method by simulating the problem of plane-wave transmission through an infinite free-standing graphene sheet with $\mu_c = 150$ meV. The FDTD spatial mesh and the time steps are set to $\Delta = \lambda_{min}/20$ and $\Delta t = \Delta/c_0$, respectively, where $\lambda_{\min}$ is the wavelength at 100 THz. The differentiated Gaussian pulse waveform

$$f(t) = (t - t_0) \exp\left\{-\beta^2 (t - t_0)^2\right\}$$

was used for temporal excitation, where $t_0 = 50$ fs and $\beta = 10/t_0$. The simulation was run for 200 000 time steps (around 100 ps). Fig. 3 shows the normalized transmitted electric field indicating that no instability was detected in the simulation. The transmission coefficient is then obtained using discrete Fourier transform and is compared with the analytical

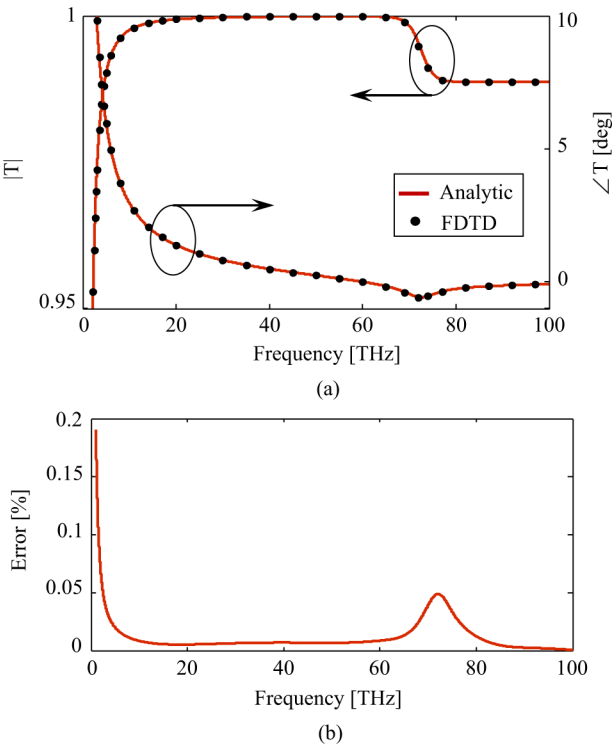

Fig. 4. (a) Transmission coefficient (T) for a normally incident plane wave through the graphene layer with $\mu_c = 150$ meV obtained by the proposed FDTD method and analytic solution. (b) The error between the FDTD simulation and analytic results.

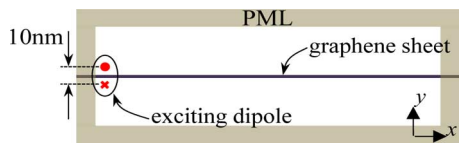

Fig. 5. Schematic of the FDTD computational domain. TM SPP on the geraphene sheet is excited by a magnetic dipole.

expression $T = 2/(2+\eta_0\sigma_g)$, where η_0 is the free-space characteristic impedance and σ_g is the surface conductivity of graphene. The comparison between the results obtained by FDTD method and analytic solution is shown in Fig. 4 demonstrating strong agreement between the two solutions such that the maximum error between them is less than 0.2% in whole frequency band of 1–100 THz.

As a second example, we simulate TM SPP surface wave on an infinite freestanding graphene layer by means of the proposed method. Fig. 2(b) clearly shows that the imaginary part of graphene conductivity can attain negative and positive values in different ranges of frequencies depending on the level of chemical potential. When $\sigma_{g,i} < 0$, a graphene layer effectively behaves as a very thin "metal" layer capable of supporting a TM SPP surface wave [15]. At 30 THz, the graphene layer with $\mu_c = 150$ meV has $\sigma_g = 7.84 \times 10^{-4} - j7.66 \times 10^{-2}$ mS, and hence it supports TM electromagnetic SPP surface wave. In the FDTD simulation, as shown in Fig. 5, the graphene sheet is positioned in the middle of the computational domain with 150×50 cells where the size of each cell is set to 7×7 nm. The time step is set to $\Delta t = \Delta/\sqrt{2}\,c_0 = 1.65 \times 10^{-17}$ s to meet the CFL stability condition. The computational space is terminated

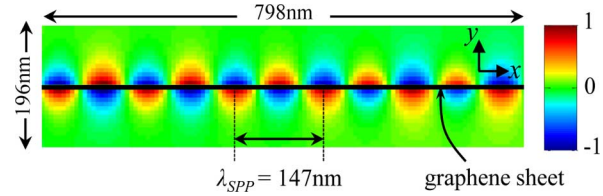

Fig. 6. Spatial distribution of E_y at time step 200 000 depicting TM SPP surface wave on the graphene layer with $\mu_c = 150$ meV. The guided wave length is extracted from the field distribution.

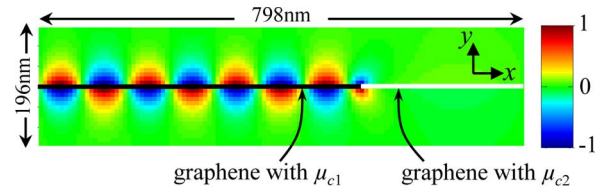

Fig. 7. Spatial distribution of E_y on the graphene layer which divided into two sections. The left section with $\mu_{c1} = 150$ meV supports TM SPP, whereas the left section $\mu_{c2} = 65$ meV does not.

by ten cells of perfectly match layer (PML) and the graphene boundary condition is extended into the PML along the x-direction to prevent spurious reflection from the boundary. A magnetic dipole (two magnetic currents with opposite directions) with a continuous sinusoidal waveform is applied for excitation at 30 THz (see Fig. 5). Notice that the symmetry used in the excitation leads to a faster steady-state response.

The spatial distribution of E_y at time step 200 000 when the fields reach steady state is shown in Fig. 6 clearly illustrating the SPP surface wave on the graphene layer. The SPP guided wavelength λ_{SPP} can be easily extracted from the steady-state field distribution, which gives us $\lambda_{\mathrm{SPP}} = 21 \times 7\,\mathrm{nm} = 147$ nm. The guided wavelength is also determined analytically using the formula $\lambda_{\mathrm{SPP}} = \lambda_0/\Re\left\{\sqrt{1-(2/\eta_0\sigma_g)^2}\right\} = 144.2$ nm [16]. We note that similar problems were simulated using the regular FDTD method in [9], where the graphene was modeled by a thin dielectric layer with a volumetric permittivity, which was approximated from the surface conductivity of graphene. In those simulations, the thickness of graphene layer was supposed to be equal to the mesh size along each direction. Hence, to obtain valid results, the mesh size had to be set very fine (around 1 nm). In our simulation, however, graphene was modeled as a SBC (not a physical layer); therefore, the FDTD mesh size was chosen around $\lambda_{\mathrm{SPP}}/20$, regardless of the physical thickness of the graphene layer. Notice the time step used in our simulation is 16.5 times larger than that used in the simulations of [9], implying significant reduction in computation resources.

As the final example, we consider TM SPP on a graphene sheet that is divided into two sections, as shown in Fig. 7. The chemical potential of the left section is set to $\mu_{c1} = 150$ meV and that of the right section is set to $\mu_{c2} = 65$ meV. At 30 THz, the surface conductivity of the left section is $\sigma_{g1} = 7.84 \times 10^{-4} - j7.66 \times 10^{-2}$ mS, which has a negative imaginary part, while that of the right side is $\sigma_{g2} = 1.62 \times 10^{-2} + j3.06 \times 10^{-2}$ mS with a positive imaginary part (see Fig. 2). Hence, the left section supports TM SPP, whereas the right section does not. Consequently, if a TM SPP is launched in the left section

towards the junction, it reflects back at that boundary line. The field distribution obtained by FDTD simulation, which is shown in Fig. 7, clearly exhibits this phenomenon, which is also illustrated in [15, Fig. 2] where graphene is modeled by a thin (1-nm-thick) conductive layer using CST Microwave Studio [29]. This phenomenon has been applied to achieve transformation optics [15] and infrared switches [30].

IV. Conclusion

This work presents a finite-difference time-domain method for modeling graphene whereby the intraband and interband terms of the surface conductivity of graphene are accounted for. This would then provide the ability to study the scattering and transmission properties of graphene over wideband in one simulation. A rational model is used to effectively approximate the surface resistivity of graphene using a new discrete-time domain surface boundary condition. The method is validated by presenting numerical examples and comparison with analytical solution. In comparison to methods available in the literature, the proposed method uses significantly less computational resources while maintaining high accuracy.

References

[1] K. S. Novoselov, V. I. Fal'ko, L. Colombo, P. R. Gellert, M. G. Schwab, and K. Kim, "A roadmap for graphene," *Nature*, vol. 490, no. 7419, pp. 192–200, Oct. 2012.

[2] A. K. Geim and K. S. Novoselov, "The rise of graphene," *Nature Mater.*, vol. 6, no. 3, pp. 183–191, Mar. 2007.

[3] A. K. Geim, "Graphene: status and prospects," *Science*, vol. 324, no. 5934, pp. 1530–1534, Jun. 2009.

[4] A. Fallahi and J. Perruisseau-Carrier, "Design of tunable biperiodic graphene metasurfaces," *Phys. Rev. B*, vol. 86, no. 19, pp. 195408–195408, Nov. 2012.

[5] R. Filter, M. Farhat, M. Steglich, R. Alaee, C. Rockstuhl, and F. Lederer, "Tunable graphene antennas for selective enhancement of THz-emission," *Opt. Express*, vol. 21, no. 3, pp. 3737–3745, Feb. 2013.

[6] W. Gao, J. Shu, C. Qiu, and Q. Xu, "Excitation of plasmonic waves in graphene by guided-mode resonances," *ACS Nano*, vol. 6, no. 9, pp. 7806–7813, Aug. 2012.

[7] Y. H. Kim, S. H. Kwon, J. M. Lee, M. S. Hwang, J. H. Kang, W. I. Park, and H. G. Park, "Graphene-contact electrically driven microdisk lasers," *Nature Commun.*, vol. 3, pp. 1123–1123, Oct. 2012.

[8] A. Mock, "Padé approximant spectral fit for FDTD simulation of graphene in the near infrared," *Opt. Mater. Express*, vol. 2, no. 6, pp. 771–781, Jun. 2012.

[9] H. Lim *et al.*, "FDTD modeling of graphene devices using complex conjugate dispersion material model," *IEEE Microw. Wireless Compon. Lett.*, vol. 22, no. 12, pp. 612–614, Dec. 2012.

[10] G. D. Bouzianas *et al.*, "Optimal modeling of infinite graphene sheets via a class of generalized FDTD schemes," *IEEE Trans. Magn.*, vol. 48, no. 2, pp. 379–382, Feb. 2012.

[11] V. Nayyeri, M. Soleimani, and O. M. Ramahi, "Modeling graphene in the finite-difference time-domain method using a surface boundary condition," *IEEE Trans. Antennas Propag.*, vol. 61, no. 8, pp. 4176–4182, 2013.

[12] A. Taflove and S. C. Hagness, *Computational Electrodynamics: The Finite-Difference Time-Domain Method.* Norwood, MA, USA: Artech House, 2000.

[13] X. Yu and C. D. Sarris, "A perfectly matched layer for subcell FDTD and applications to the modeling of graphene structures," *IEEE Antennas Wireless Propag. Lett.*, vol. 11, pp. 1080–1083, 2012.

[14] V. P. Gusynin, S. G. Sharapov, and J. P. Carbotte, "Magneto-optical conductivity in graphene," *J. Phys., Conden. Matter*, vol. 19, no. 2, pp. 026222–026222, Jan. 2007.

[15] A. Vakili and N. Engheta, "Transformation optics using graphene," *Science*, vol. 332, no. 6035, pp. 1291–1294, Jun. 2011.

[16] G. W. Hanson, "Dyadic Green's functions and guided surface waves for a surface conductivity model of graphene," *J. Appl. Phys.*, vol. 103, no. 6, pp. 064302–064302, Mar. 2008.

[17] M. Han, R. W. Dutton, and S. Fan, "Model dispersive media in finite-difference time-domain method with complex-conjugate pole-residue pairs," *IEEE Microw. Wireless Compon. Lett.*, vol. 16, no. 3, pp. 119–121, Mar. 2006.

[18] G. W. Hanson, "Dyadic green's functions for an anisotropic, non-local model of biased graphene," *IEEE Trans Antennas Propag.*, vol. 56, no. 3, pp. 747–757, Mar. 2008.

[19] B. Gustavsen and A. Semlyen, "Rational approximation of frequency domain responses by vector fitting," *IEEE Trans. Power Del.*, vol. 14, no. 3, pp. 1052–1061, Jul. 1999.

[20] E. C. Levi, "Complex-curve fitting," *IRE Trans. Autom. Control*, vol. 4, no. 1, pp. 37–44, May 1959.

[21] G. Kobidze, "Implementation of collocated surface impedance boundary conditions in FDTD," *IEEE Trans. Antennas Propag.*, vol. 58, no. 7, pp. 2394–2403, Jul. 2010.

[22] L. A. Falkovsky and A. A. Varlamov, "Space-time dispersion of graphene conductivity," *Eur. Phys. J. B*, vol. 56, no. 4, pp. 281–284, Apr. 2007.

[23] G. Lovat, P. Burghignoli, and R. Araneo, "Low-frequency dominant-mode propagation in spatially dispersive graphene nanowaveguides," *IEEE Trans. Electromagn. Compat.*, vol. 55, no. 2, pp. 328–333, Apr. 2013.

[24] J. S. Gomez-Diaz, J. R. Mosig, and J. Perruisseau-Carrier, "Effect of spatial dispersion on surface waves propagating along graphene sheets," *IEEE Trans. Antennas Propag.*, vol. 61, no. 7, pp. 3589–3596, Jul. 2013.

[25] D. L. Sounas and C. Caloz, "Gyrotropy and nonreciprocity of graphene for microwave applications," *IEEE Trans. Microw. Theory Tech.*, vol. 60, no. 4, pp. 901–914, Apr. 2012.

[26] D. L. Sounas *et al.*, "Faraday rotation in magnetically biased graphene at microwave frequencies," *Appl. Phys. Lett.*, vol. 102, no. 19, pp. 191901–191901, May 2013.

[27] N. Chamanara, D. Sounas, and C. Caloz, "Non-reciprocal magnetoplasmon graphene coupler," *Opt. Express*, vol. 21, no. 9, pp. 11248–11256, May 2013.

[28] M. Jablan, H. Buljan, and M. Soljacic, "Plasmonics in graphene at infrared frequencies," *Phys. Rev. B*, vol. 80, no. 24, pp. 245435–245435, Dec. 2009.

[29] CST Studio Suite [Online]. Available: http://www.cst.com

[30] J. S. Gomez-Diaz and J. Perruisseau-Carrier, "Graphene-based plasmonic switches at near infrared frequencies," *Opt. Express*, vol. 21, no. 13, pp. 15490–15504, Jul. 2013.

Vahid Nayyeri (S'08) was born in Tehran, Iran, in 1983. He received the B.Sc. degree from the Iran University of Science and Technology (IUST), Tehran, Iran, in 2006 and the M.Sc. degree from the University of Tehran, Tehran, Iran, in 2008, both in electrical engineering. Since 2008, he has been working toward the Ph.D. degree in electrical engineering at IUST.

He worked for the IUST research center as a RF-circuit designer from 2007 to 2010. He was then the technical manager of three research and industrial projects at the Antenna Research Laboratory of IUST from 2010 to 2012. In September 2012, he joined the University of Waterloo as a Visiting Scholar. He has authored and coauthored one book (in Persian) and more than 20 journal and conference papers. His research interests include theoretical and computational electromagnetics (especially finite-difference time-domain method).

Mr. Nayyeri has served as reviewer to the IEEE Transactions on Antennas and Propagation and the IEEE Transactions on Microwave Theory and Techniques.

Mohammad Soleimani received the B.Sc. degree in electrical engineering from the University of Shiraz, Shiraz, Iran, in 1978 and the M.Sc. and Ph.D. degrees from Pierre and Marie Curio University, Paris, France, in 1981 and 1983, respectively.

He is a Professor with the Iran University of Sciences and Technology, Tehran, Iran. He has also served in many executive and research positions. He has authored and coauthored 19 books (in Persian) and more than 150 journal and conference papers. His research interests include electromagnetics, high-frequency electronics, and antennas.

Omar M. Ramahi (F'09) was born in Jerusalem, Palestine. He received the B.S. degrees in mathematics and electrical and computer engineering (*summa cum laude*) from Oregon State University, Corvallis, OR, USA, and the Ph.D. degree in electrical and computer engineering from the University of Illinois at Urbana-Champaign under the supervision of Prof. R. Mittra.

He held postdoctoral and visiting fellowship positions at the University of Illinois at Urbana-Champaign under the supervision of Prof. Y. T. Lo and Prof. R. Mittra. He then worked at Digital Equipment Corporation (presently, HP), where he was a member of the Alpha Server Product Development Group. In 2000, he joined the faculty of the James Clark School of Engineering at the University of Maryland, College Park, MD, USA, as an Assistant Professor and later as a tenured Associate Professor. At Maryland, he was also a faculty member of the CALCE Electronic Products and Systems Center. He is currently a Professor in the Electrical and Computer Engineering Department, University of Waterloo, ON, Canada. He holds cross appointments with the Department of Mechanical and Mechatronics Engineering and the Department of Physics and Astronomy. He has authored and coauthored more than 300 journal and conference technical papers on topics related to the electromagnetic phenomena and computational techniques to understand the same. He is a coauthor of the book *EMI/EMC Computational Modeling Handbook* (1st ed.: Kluwer, 1998; 2nd ed.: Springer-Verlag, 2001; Japanese ed. published in 2005).

Prof. Ramahi is the winner of the 1994 Digital Equipment Corporation Cash Award, the 2004 University of Maryland Pi Tau Sigma Purple Cam Shaft Award for teaching, the Excellent Paper Award in the 2004 International Symposium on Electromagnetic Compatibility, Sendai, Japan, and the 2010 University of Waterloo Award for Excellence in Graduate Supervision. In 2012, he received the IEEE Electromagnetic Compatibility Society Technical Achievement Award. He served as a consultant to several companies and was a co-founder of EMS-PLUS, LLC and Applied Electromagnetic Technology, LLC, and the Eastern Rugs and Gifts Company. In 2009, he served as a Co-Guest Editor for the *Journal of Applied Physics* Special Issue on Metamaterials and Photonics. From 2009 to 2011, He served as IEEE EMC Society Distinguished Lecturer. Presently, he is serving as an Associate Editor for the IEEE TRANSACTIONS ON COMPONENTS, PACKAGING AND MANUFACTURING TECHNOLOGY.